HEART Aerothermodynamic Analysis

Alireza Mazaheri
Langley Research Center, Hampton, Virginia

May 2012

NASA STI Program . . . in Profile

Since its founding, NASA has been dedicated to the advancement of aeronautics and space science. The NASA scientific and technical information (STI) program plays a key part in helping NASA maintain this important role.

The NASA STI program operates under the auspices of the Agency Chief Information Officer. It collects, organizes, provides for archiving, and disseminates NASA's STI. The NASA STI program provides access to the NASA Aeronautics and Space Database and its public interface, the NASA Technical Report Server, thus providing one of the largest collections of aeronautical and space science STI in the world. Results are published in both non-NASA channels and by NASA in the NASA STI Report Series, which includes the following report types:

- TECHNICAL PUBLICATION. Reports of completed research or a major significant phase of research that present the results of NASA Programs and include extensive data or theoretical analysis. Includes compilations of significant scientific and technical data and information deemed to be of continuing reference value. NASA counterpart of peer-reviewed formal professional papers, but having less stringent limitations on manuscript length and extent of graphic presentations.

- TECHNICAL MEMORANDUM. Scientific and technical findings that are preliminary or of specialized interest, e.g., quick release reports, working papers, and bibliographies that contain minimal annotation. Does not contain extensive analysis.

- CONTRACTOR REPORT. Scientific and technical findings by NASA-sponsored contractors and grantees.

- CONFERENCE PUBLICATION. Collected papers from scientific and technical conferences, symposia, seminars, or other meetings sponsored or co-sponsored by NASA.

- SPECIAL PUBLICATION. Scientific, technical, or historical information from NASA programs, projects, and missions, often concerned with subjects having substantial public interest.

- TECHNICAL TRANSLATION. English-language translations of foreign scientific and technical material pertinent to NASA's mission.

Specialized services also include organizing and publishing research results, distributing specialized research announcements and feeds, providing information desk and personal search support, and enabling data exchange services.

For more information about the NASA STI program, see the following:

- Access the NASA STI program home page at *http://www.sti.nasa.gov*

- E-mail your question to help@sti.nasa.gov

- Fax your question to the NASA STI Information Desk at 443-757-5803

- Phone the NASA STI Information Desk at 443-757-5802

- Write to:
  STI Information Desk
  NASA Center for AeroSpace Information
  7115 Standard Drive
  Hanover, MD 21076-1320

NASA/TM–2012-217568

HEART Aerothermodynamic Analysis

Alireza Mazaheri
Langley Research Center, Hampton, Virginia

May 2012

Abstract

This paper presents an assessment of the aerothermodynamic environment around an 8.3 meter High Energy Atmospheric Reentry Test - (HEART) vehicle. This study generated twelve nose shape configurations and compared their responses at the peak heating trajectory point against the baseline nose shape. The heat flux sensitivity to the angle of attack variations are also discussed. The possibility of a two-piece Thermal Protection System (TPS) design at the nose is also considered, as are the surface catalytic affects of the aeroheating environment of such configuration. Based on these analyses, an optimum nose shape is proposed to minimize the surface heating. A recommendation is also made for a two-piece TPS design, for which the surface catalytic uncertainty associated with the jump in heating at the nose-IAD juncture is reduced by a minimum of 93%. In this paper, the aeroshell is assumed to be rigid and the inflatable fluid interaction effect is left for future investigations.

Nomenclature

c	Mass fraction
C_p	Specific heat, $J/kg.K$
D	Diffusion coefficient, m^2/sec
G	Gibbs free energy, m^2/sec^2
h	Enthalpy, J/kg
K	Equilibrium constant
k	Conductivity, $W/m.K$
k'	Recombination rate constant
m	Species mass, kg
Le	Lewis number
M_w	Molecular weight, kg
P	Pressure, Pa
q	Heat flux, W/m^2
$\bar{R}$	Universal gas constant, $m^2/sec^2.K$
Sc	Schmidt number
T	Temperature, K
U	Total velocity, m/sec
$\dot{w}$	Production rate, $kg/m^3.sec$
α	angle of attack, deg, or Stoichiometric coefficient, or Mass fraction
β	Velocity gradient, $1/sec$, or Stoichiometric coefficient
γ	Catalytic efficiency, recombination coefficient
ϵ	Geometry related parameter
κ	Boltzmann constant, $m^2/sec^2. kg/K$
θ	Temperature ratio, T/T_e
μ	Viscosity, $kg/m.sec$
χ	Mole fraction

ρ	Mixture density, kg/m^3
ω	Recombination rate temperature exponent

Subscripts
e	edge
$diff$	diffusion or catalytic
w	wall
s	species s

1   Introduction

Hypersonic inflatable aerodynamic decelerators (HIAD) [1] are being developed for next generation atmospheric entry vehicles. Inflatables offer increased payload volume in a fraction of the launch vehicle shroud and have the potential to deliver more payload mass to the surface for a given set of trajectory constraints compared to rigid aeroshells. Another advantage is that the inflatable aerodynamic decelerators (IAD) [2] also allow access to the payload after the vehicle is integrated for launch.

IADs are still in the developmental phase with technical challenges still to be resolved. These challenges include the aerothermodynamic environment and the associated thermal protection systems (TPS) response of the IAD during atmospheric entry. The Inflatable Reentry Vehicle Experiment (IRVE)-III is addressing one of the steps on the development path of the HIAD, which is a more operationally realistic flight environment than its predecessor IRVE-II [3]. The High Energy Atmospheric Reentry Test (HEART), which will build on the IRVE flights and developments, focuses on understanding the scale effects of an IAD. HEART is proposed to be an 8.3m HIAD entering the Earth ballistically from the International Space Station (ISS) as a mean to bring back unnecessary or excess payload (e.g. space junk or garbage) from the ISS.

For this study, baseline HEART geometry was analyzed and optimized for its aeroheating environment during the Earth entry. For the shape optimization, the author considered several nose-IAD shapes and proposes an optimum configuration. The effects of angle of attack on the surface aeroheating are also analyzed. Ranges of TPS surface catalytic coefficients are considered and a recommendation is made in order to mitigate the catalytic uncertainty. Note that in this paper, the aeroshell is assumed to be rigid and the inflatable fluid interaction effect that becomes important mainly in the low supersonic part of the trajectory is left for future investigations.
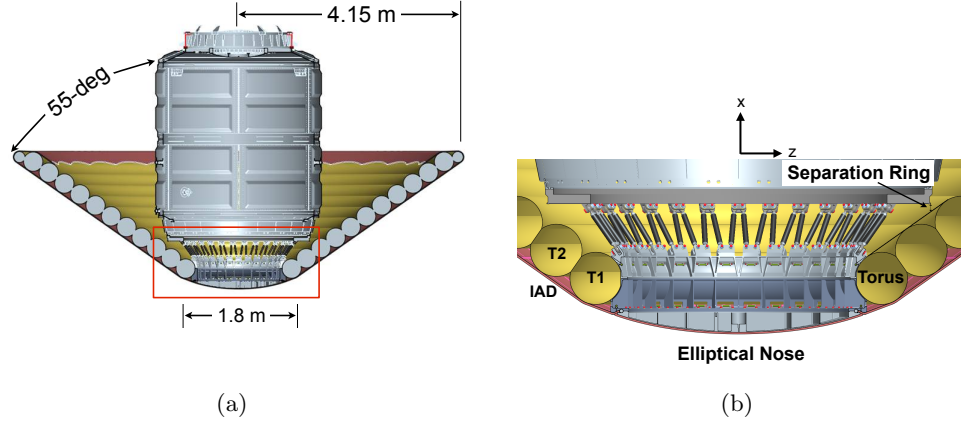
Figure 1. Baseline geometry for a) 8.3-meter HEART geometry with a 55° half-angle cone, and b) close-up around the nose.

2   Baseline Configuration

This section discusses an aeroheating analysis conducted on the HEART baseline geometry, which consisted of an elliptical nose attached to an 8.3-m diameter IAD with a 55° half-angle cone. Figure 1 schematically shows the HEART geometry. The rigid nose piece, which is elliptical for packaging purposes, creates a juncture at the first IAD torus, known as T1. In this baseline configuration, a TPS material wraps around the outer surfaces of the IAD and the nose entirely.

This paper presents an aerothermodynamic environment analysis on this baseline geometry to identify the peak heating point along the trajectory. The trajectory that was used in these simulations is plotted in Figure 2. Table 1 shows the tabulations of the free-stream conditions for the selected points shown as open symbols in Figure 2. This study assumed laminar 5-species air with thermal equilibrium condition. Surface temperature was computed using a radiative equilibrium boundary condition with an assumed constant emissivity of 0.85. The surface catalytic condition was assumed to be fully-catalytic (FC), in which all atoms were allowed to recombine on the surface. This condition provided the upper bound for the surface heat flux. Unless otherwise stated, the computations were performed using the LAURA-5 [4] code at a constant angle of attack of 10-deg. LAURA has been used on other vehicles, such as Fire II [5], the Space Shuttle Orbiter [6, 7], and X-37, and is also being used for Mars Science Laboratory (MSL) [8] and Multi-Purpose Crew Vehicle (MPCV) missions [9].

Figure 3 shows the centerline surface heat flux for the baseline geometry at the trajectory points T2163–T2292. These solutions were per-
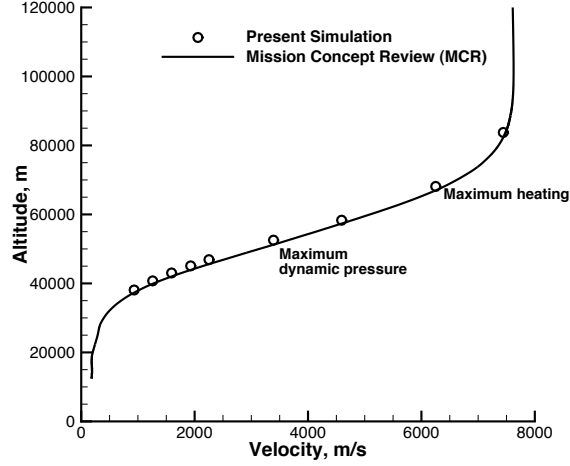
Figure 2. Trajectory points used in the present simulation.

Table 1. Freestream conditions for the trajectory points shown in Figure 2.

Time, sec	Altitude, km	$\rho_\infty, kg/m^3$	$U_\infty, m/sec$	T, K	Mach
2163	84	8.912E-06	7443.7	213.3	25
2255	68	8.914E-05	6252.0	224.6	21
2292	58	3.383E-04	4592.9	241.3	15
2311	52	7.056E-04	3391.2	253.4	11
2328	47	1.458E-03	2252.9	257.3	7
2334	45	1.848E-03	1930.2	256.9	6
2340	43	2.471E-03	1593.5	252.3	5
2348	41	3.434E-03	1260.1	247.0	4
2356	38	5.087E-03	932.9	240.3	3

formed on two separate three-dimensional structured grids, both with the same number of surface points but with a factor of two difference in the number of points normal to the body. Doubling the number of points did not change the surface heat flux values more than 5% and therefore the solutions were confirmed to be grid-converged. The results in Figure 3 showed that the surface heating increases from the point T2163 to T2255 before it decreased at point T2292. The point T2255, which was a Mach 21 point on the entry trajectory, was therefore the peak heating point for this trajectory. This trajectory does not have a dual-peak pulse and thus no further analysis is needed to locate the peak heating condition.

The centerline surface heating profile, however, presented a double peak heating, which was due to the rapid curvature change from the nose to the IAD section (see Figure 1) Note that simulations were conducted
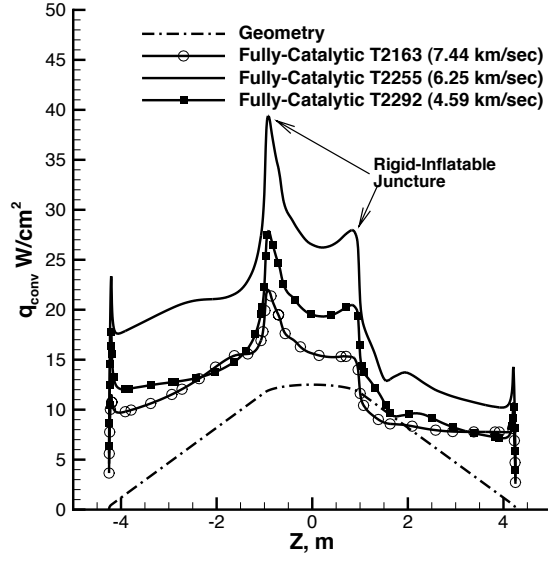
Figure 3. Centerline surface heat flux on the baseline geometry.

at $\alpha = 10°$. The nose-IAD juncture closest to the stagnation point pro-
duced a significant rise in the surface heat flux. The maximum surface
heat flux at this peak heating point, T2255, was about 40 W/cm^2. The
uneven distribution flattened out as the vehicle traveled down the tra-
jectory, but its presence was not desirable as this could constrain the
vehicle design from further considerations. For example, because the
IAD is not rigid the TPS fabric would have some irregularity between
the tori, which is known as TPS scalloping. The TPS scalloping, itself,
could cause some irregularity to the surface heat flux. However, if the
smooth surface heat distribution were uneven, the TPS scalloping could
augment the surface heating. Thus, it is desirable to have a geometry
that produces a relatively smooth surface heating profile but still fulfills
packaging constraints.

The surface catalytic contribution to convective heat flux is calcu-
lated by comparing the fully-catalytic surface heat flux to one computed
with a non-catalytic (NC) surface condition. The non-catalytic surface
is defined as a surface that does not allow species recombinations at the
surface. A non-catalytic surface eliminates the catalytic heating portion
of the heat flux and results in a much lower heat flux than that pro-
duced by a fully-catalytic surface. This effect is illustrated in Figure 4,
which shows a factor of three in catalytic uncertainty. The difference in
heat flux due to catalysis was highest at the peak heating and decreased
rapidly at lower altitudes. For example, the catalytic uncertainty factor
decreased from about 3 to about 2 at the next trajectory point after the
peak heating point (Figure 5). In Figure 5, a code to code comparison
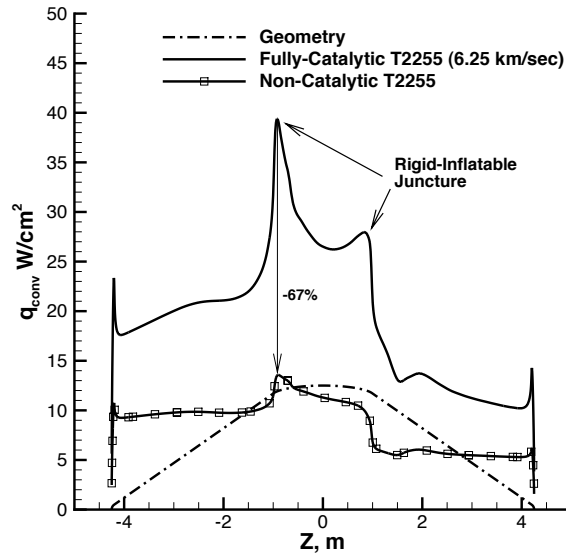
5

Figure 4. Maximum surface catalytic uncertainty for the surface heat flux on the baseline geometry.
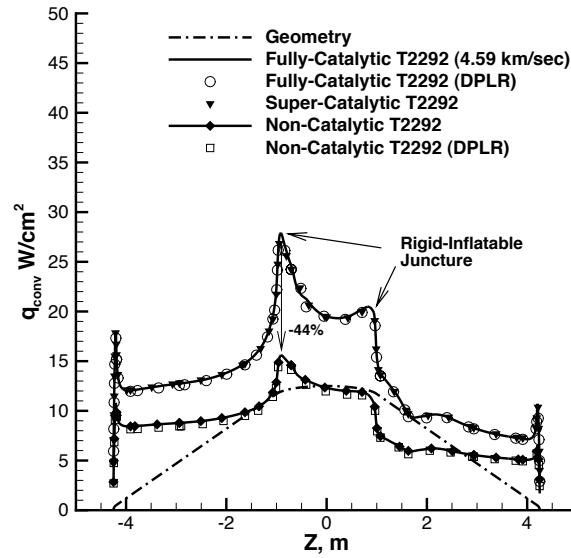

Figure 5. Catalytic uncertainty for the surface heat flux on the baseline geometry at T2292.

was made and excellent agreement was achieved between the LAURA-5 [4] and the DPLR [10] codes. In this comparison, the grid was first adapted and aligned with the bow shock using the LAURA-5 code. The same adapted grid was then used for the DPLR runs with no additional grid alignment.

Figure 5 also shows a LAURA-5 super-catalytic solution. The super-catalytic condition was defined by replacing the species concentration at the wall with the freestream species compositions. The comparison showed that the fully-catalytic and the super-catalytic results were almost identical. This means that the 100% catalytic efficiency at the wall resulted in the same species concentration as the freestream because of a relatively a low surface temperature. The author observed similar results for the other trajectory points.

The trajectory point T2311 is the maximum dynamic pressure point. The corresponding pressure contour plot is shown in Figure 6. In a subset of Figure 6, the adapted grid is shown. A wall cell Reynolds number of 0.1 was imposed during the adaptation process. During the adaptation process the grid was refined across the shock discontinuity for a crisper shock location prediction and better numerical accuracy.

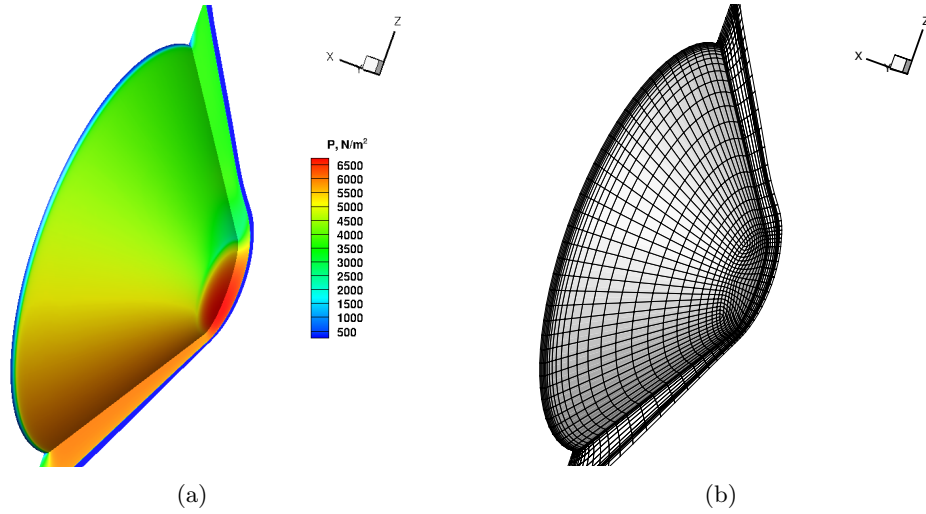(a)   (b)

Figure 6. a) Pressure contour plot at the maximum pressure point on the baseline geometry and b) Structure grid used in the simulation (for clarity every 4th grid points is shown.)

3 Nose Shape Optimization

The aeroheating analysis of the baseline HEART geometry presented in the previous section showed an unevenness in the surface heat flux, more specifically a double peak heating at the nose-IAD juncture. This section presents a series of nose optimizations to reduce the surface heat flux and

achieve a relatively smoother surface heating profile. The optimization was done manually and sequentially. The nose shapes were modified through a series of tries and errors according to their surface heat flux responses. There were some geometrical constraints from packaging and manufacturing standpoints that were imposed before the optimization. At the beginning of the investigation, there was a constraint that the IAD should clear the separation ring at the shoulder, shown in Figure 1. The baseline configuration, shown in Figure 1, had the IAD clearing this shoulder by just over 2 inches. However, it was expected that the IAD would deflect under its load such that the IAD would contact the shoulder. Therefore, it was suggested to move the IAD back to where it would touch the shoulder when it had no load. This provided an additional 2 inches in the direction of the minor diameter of the baseline nose.

During early optimization, the backside portion of the IAD section was allowed to curve. Initially, this was not a constraint, but it was suggested that any curvature to the IAD section would complicate the fabrication process, and thus must be avoided. The overall vehicle diameter of 8.3 m and the half-angle cone of 55-deg were also fixed to limit the parameters.

Figure 7 shows a series of the nose shapes conducted on the HEART baseline geometry. The dotted lines correspond to the baseline config-
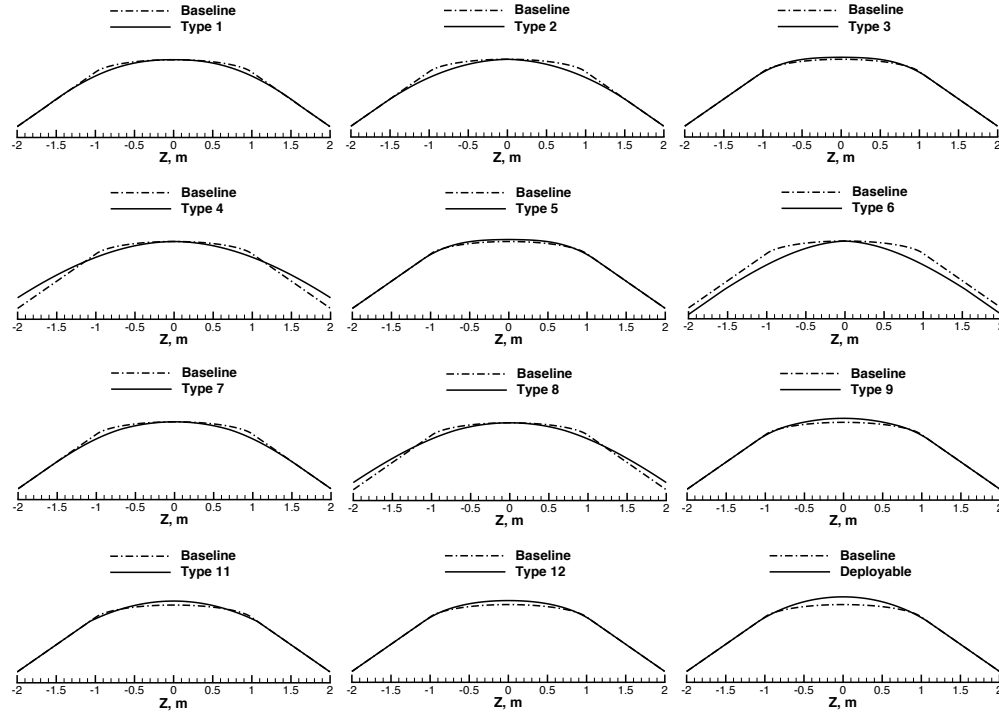

Figure 7. Series of nose shape optimizations for the 8.3 m HEART vehicle with 55-deg half-angle cone.

uration while the solid lines represent alternative geometries. Some of the modified geometries require slightly curved IADs, but not beyond the fourth torus, T4, and some had the exact same IAD section as the baseline. Nose shapes that were elliptical did not have an analytical representation as they were generated based on past experiences and examination of the surface heating profile of the baseline geometry.

Separate three dimensional (3D) structured grids were generated for each of the Types 1–12 geometries. To do a better comparison with the baseline geometry, the surface grids were kept as close to the baseline grid as possible. The total number of volume cells was also kept identical. During the simulation, the grids were adapted, aligned and clustered around the bow shock, similar to the one shown in Figure 6b.

Only the peak heating point, T2255, with a fully-catalytic surface and radiative equilibrium boundary condition is discussed here. The geometry effects were based on the surface heating distribution and its maximum value as compared to the baseline geometry. Among the presented configurations, Types 5, 9, 11, 12, and the deployable nose concept did not require any changes to the IAD curvature. The remaining geometries added relatively small curvature to the IAD section up to the forth torus, T4. Types 5, 9, and 12 were non-spherical, semi-elliptical nose configurations. All others were spherical. Types 9 and 11 had a nose that was moved, respectively, one and two inches forward compared with the baseline geometry. Type 12 was similar to Type 11 except that the nose was no longer spherical. The center point of the Type 12 nose was about 2 inches forward relative to the baseline geometry.

One of the interesting configurations studied here is the deployable nose concept proposed by Hughes [11]. In this concept, illustrated schematically in Figure 8, the nose is deployed from a stowed position at the entry point, which stretches the TPS fabric. This would provide a smaller nose radius; and, therefore the surface would be expected to experience a higher heat flux. However, the available unused room behind the deployed nose could be used as heat sink. The deployed nose, which is spherical, pushes the nose four inches forward with respect to the baseline grid. The deployable nose may impose some mechanical complexity that is beyond the scope of this paper and therefore is not addressed here.

Figure 9 represents the centerline surface heat flux for all the above geometries. A more detailed comparison is summarized and tabulated in Table 2. According to this table, all the modified geometries, except Type 6, provided a 11–26% reduction in surface heating compared with the baseline geometry. Type 6 produced a slightly higher surface heat flux than the baseline geometry. All the modified geometries also experienced a $4 - 6\%$ decrease in surface temperature.

The results summarized in Table 2 show that Types 4 and 8 provided the best surface heat flux responses. However, both Types 4 and 8 added curvatures to the IAD section up to T2 and were the choice
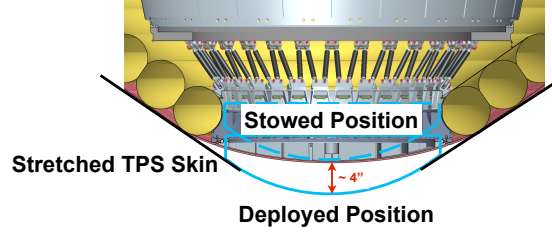
Figure 8. Deployable concept for the HEART geometry [11].

Table 2. Maximum surface heat flux and percent reduction compare to
the baseline nose. Note: $\alpha = 10°$.

Type	$q_{max}, W/cm^2$	T_{max}, K	$1 - \frac{q_{baseline}}{q}$	$1 - \frac{T_{baseline}}{T}$	Curved IAD?	Nose Shape
Baseline	39	1690	-	-	No	Ellitical
1	32	1600	-0.22	-0.06	T1-T2	Spherical
2	34	1630	-0.15	-0.04	T1-T2	Spherical
3	34	1630	-0.15	-0.04	T1-T2	Spherical
4	31	1600	-0.26	-0.06	T1-T2	Spherical
5	34	1630	-0.15	-0.04	No	Elliptical
6	41	1710	0.05	0.01	T1-T3	Spherical
7	34	1630	-0.15	-0.04	T1-T2	Spherical
8	33	1620	-0.18	-0.04	T1-T4	Spherical
9	34	1630	-0.15	-0.04	No	Spherical
11	33	1620	-0.21	-0.04	No	Spherical
12	34	1630	-0.15	-0.04	No	Elliptical
Deployable	35	1650	-0.11	-0.04	No	Spherical

(a) Type 1   (b) Type 2   (c) Type 3

(d) Type 4   (e) Type 5   (f) Type 6

(g) Type 7   (h) Type 8   (i) Type 9

(j) Type 11   (k) Type 12   (l) Deployable
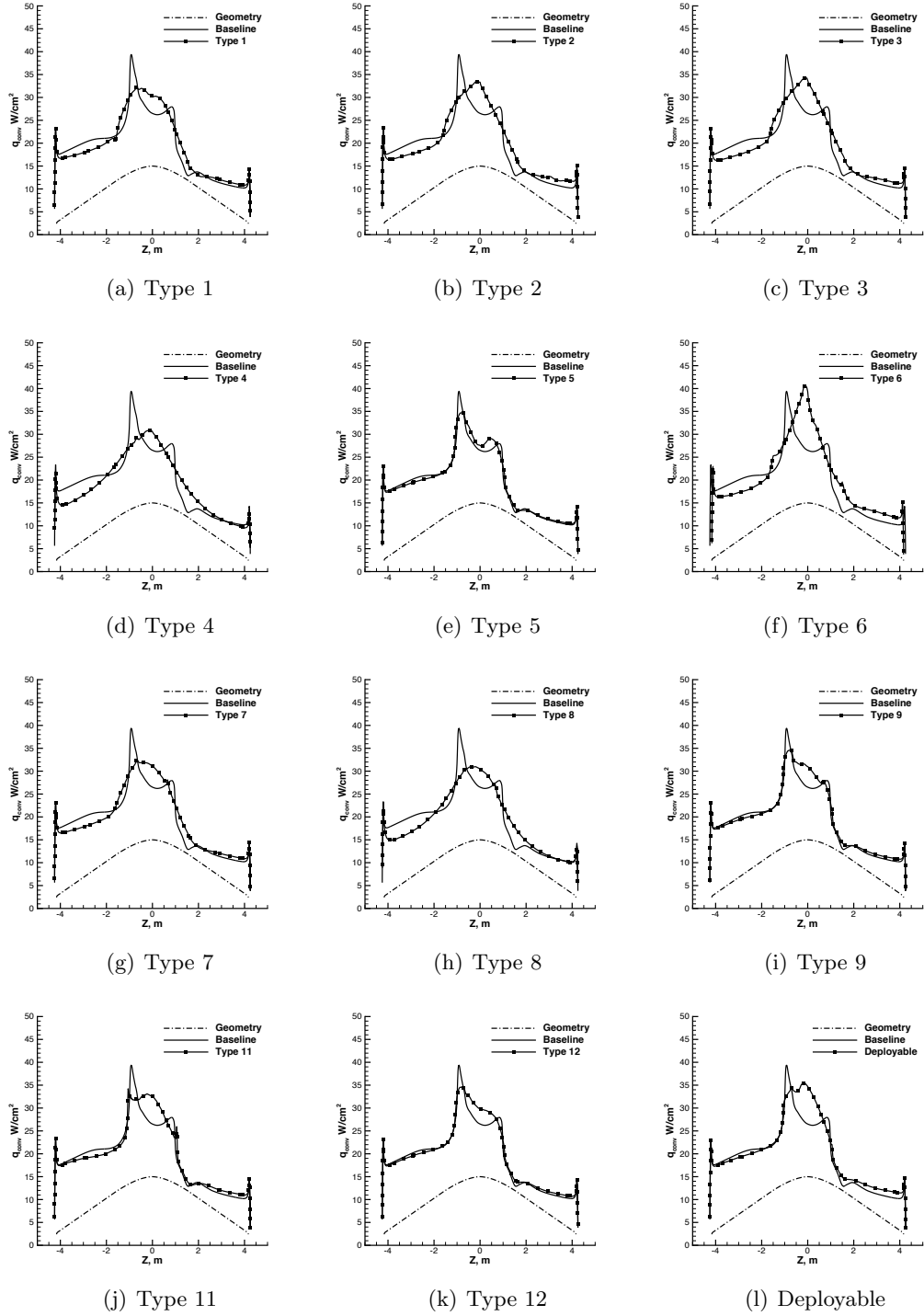
Figure 9. Centerline heating distribution for the nose shape configurations presented in the Figure 7. Note: $\alpha = 10°$.

amongst the curved IAD configurations. Types 11 and 12, on the other hand, bounded all the specified constraints and were the preferred choices within the straight IAD configurations. Type 12 provided a relatively smoother surface heating flux distribution and therefore was selected as the optimum geometry. The nose shape of the Type 12 geometry between $z = \pm 1$ m can be expressed by a fourth order polynomial as $x = -0.0514 - 0.000143z + 0.147z^2 - 0.000138z^3 + 0.0684z^4$.

4 Angle of Attack Effects

The HEART trajectory is ballistic with angle of attack variations of about $\pm$ 5 degrees. To account for the worst case, the optimizations were performed at an angle of attack (in this case $\alpha = 10$) at which the vehicle experienced a maximum surface heating. In this section the sensitivity of heating to the variations in the angle of attack is studied.

In the previous section, the shape optimization revealed that Type 12, which did not require modification to the IAD section of the baseline geometry, experiences the lowest maximum surface heating among the fixed IAD geometries studied. For this reason, only this type is presented and analyzed in this section. Figure 10 shows the results of the angle of attack effect on surface heating. Open symbols in Figure 10 indicate
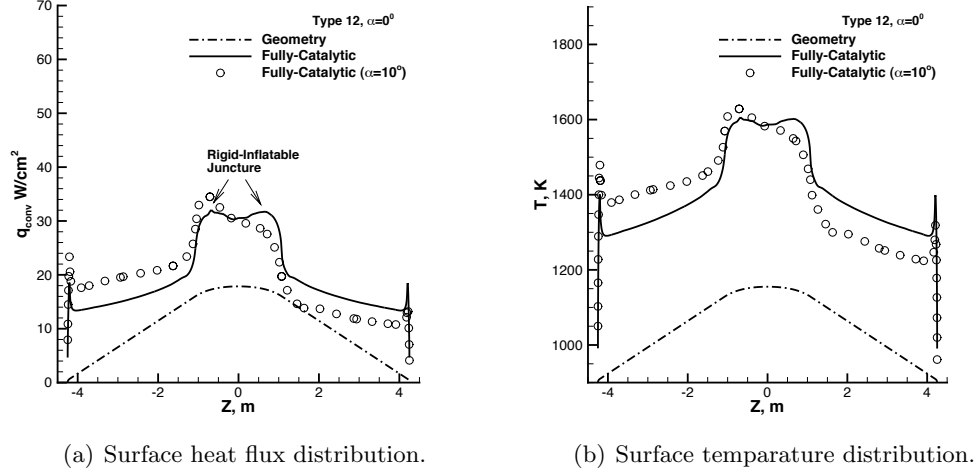

(a) Surface heat flux distribution.   (b) Surface temparature distribution.

Figure 10. angle of attack effects on the Type 12 geometry.

the solutions at $\alpha = 10°$ with a fully-catalytic surface. The solid lines indicate solutions at $\alpha = 0°$. The results showed a relatively minor heat flux sensitivity to the entry angle, meaning that additional aeroheating analysis might not be needed to account for the angle of attack variations during the entry. This was because the Type 12 provided a relatively uniform nose curvature within $\pm$ 10 degrees relative to the free stream velocity. Thus, the angle of attack effects on the surface heating predic-

tion were minor. Note that the maximum surface heating of 34 W/cm^2 had been reduced by about 10% with reduction of α. Similar results were seen for surface temperature. The IAD surface also experienced slightly lower surface heat flux and temperature at $\alpha = 0$.

5 Catalytic Surface Effect

The HEART inner mold line (IML) must be protected with TPS material to survive the entry environment. The fabric TPS catalytic characteristics that will cover the IAD surface are yet to be determined. In this section, an assessment is made for a two-piece nose-IAD configuration using the Type 12 (optimum) geometry, where the nose was made of a separate non-ablative TPS material. The IAD was still wrapped with a TPS fabric. Thus, the nose probably would have a surface catalytic property that is not necessarily similar to the IAD TPS. This configuration was, therefore, subject to an aerothermodynamic phenomenon known as *catalytic jump.*

Maximum catalytic uncertainty at the peak heating condition defined as the difference in fully- and non-catalytic heating rates was about 250% for the Type 12 geometry with a fully wrapped TPS fabric (Figure 11). The uncertainty translated to about 20 W/cm^2 variations in surface heating from a non-catalytic to a fully-catalytic surface condition. Note that at this entry condition, the fully-catalytic and super-catalytic conditions were predicting similar surface heating as presented previously in Figure 5.

For the two-piece nose-IAD catalytic jump analysis, the nose was assumed to be non-catalytic. This provided the worst catalytic jump condition as all the atomic species present above the nose surface would be available for recombination on the IAD surface. The availability of free atoms above a catalytic surface caused a rapid jump in surface heating as a result of additional recombination energy.

The IAD surface catalysis was varied from a low catalytic to a fully catalytic condition. Among these different surface catalyses a surface with a variable catalytic property (such as Reaction Cured Glass (RCG), which was used on the Space Shuttle Orbiter tiles) was also considered. Figure 12 shows the variation of RCG-catalytic efficiency with the temperature.

Surface catalytic efficiency (γ), whether it was constant or variable, was used in the computation of the wall catalytic species recombination rate constant, defined as [12, 18]

$$k_{ws} = \frac{2\gamma_s}{2 - \gamma_s} \sqrt{\frac{\kappa T_w}{2\pi m_s}} \tag{1}$$

The computations were conducted at the peak heating condition and $\alpha = 0°$. Figure 13 shows plots of surface heat flux and temperature
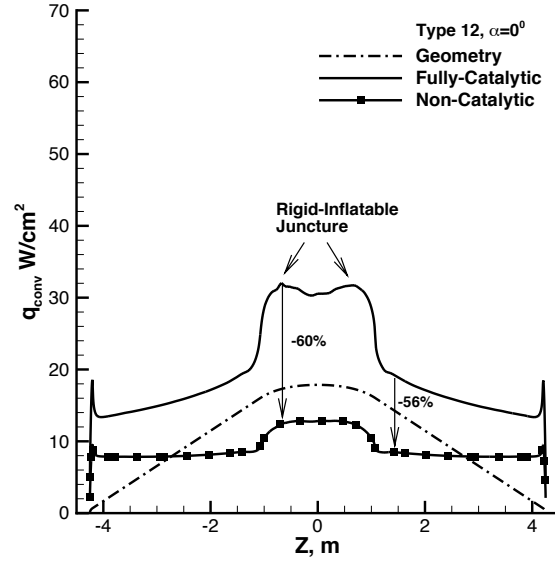
13

Figure 11. Maximum catalytic uncertainty at the peak heating condition for the Type 12 geometry wrapped entirely with a fabric TPS.
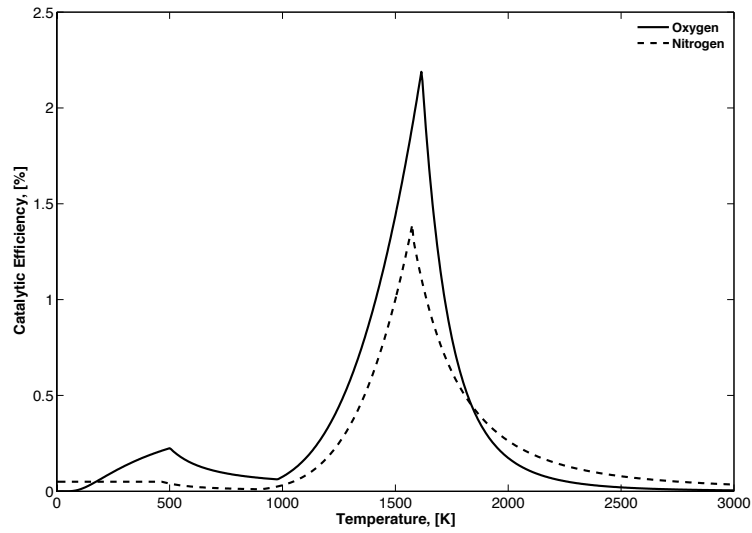

Figure 12. RCG-Catalytic efficiency with temperature.

Table 3. Summary of the catalytic jump analysis for the Type 12 geometry with a non-catalytic nose at the peak heating condition and $\alpha = 0°$.

IAD Catalysis (γ)	$q_{max}, W/cm^2$	T_{max}, K	MCAF	MTAF
0.00	12.8	1278	1.00	1.00
0.01	24.3	1500	1.89	1.17
RCG	26.8	1530	2.08	1.20
0.03	39.5	1690	3.07	1.32
0.05	46.6	1760	3.62	1.38
0.10	54.5	1830	4.24	1.43
1.00	66.6	1920	5.19	1.50

along the center body of the geometry. The solid lines represent solutions with a uniform fully-catalytic nose-IAD surface. Solutions with a uniform non-catalytic nose-IAD surface are shown with closed squares. Open circles with solid lines are the solutions with non-catalytic nose and partially catalytic IAD. The surface heat flux is presented in the plots in the left column. The plots shown in the right column are for the surface temperature.

The results showed that a 1% catalytic jump ($\gamma = 0.01$) leads to about 170% increase in the surface heat flux at the nose-IAD juncture above the non-catalytic (NC) value. The heat flux then recovered to about 76% above the non-catalytic surface results on the IAD section, which corresponded to about 15 W/cm^2. The surface temperature jump was not as severe; 27% at the nose-IAD juncture and 14% on the IAD section.

Results for an IAD with a RCG-catalytic surface predicted a 161% jump in the surface heat flux and a 23% jump in the surface temperature. These were slightly higher than the values predicted for the 1% catalytic jump. However, both the surface heat flux and the temperature values recovered to about 42% and 8% of the non-catalytic IAD results, respectively. The results with IAD surface catalytic efficiencies of 0.03, 0.05, 0.1, and 1.0 showed surface heat flux jumps of 252, 316, 397, and 520% above the non-catalytic value, respectively. The surface temperature jumps were, respectively, 35, 40, 46, and 54% higher than the values predicted with a uniform non-catalytic surface. However, results for the IAD surface catalysis above 5% recovered to the almost fully-catalytic value on the IAD section (See the Appendix A for more discussion on this.) The results of surface catalytic efficiency of up to 3% were bound within the maximum catalytic uncertainly prediction, meaning they were not above the uniform fully-catalytic nose-IAD surface. Surface catalysis higher than $\gamma = 0.03$ produced a jump that was significantly higher than the stagnation point for the fully-catalytic surface. The results are further summarized and tabulated in Table 3. In this table the maximum catalytic augmentation factor, MCAF, and the
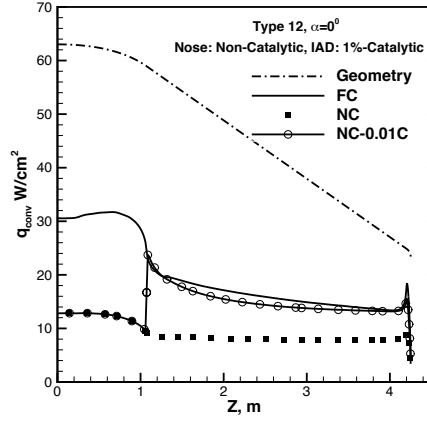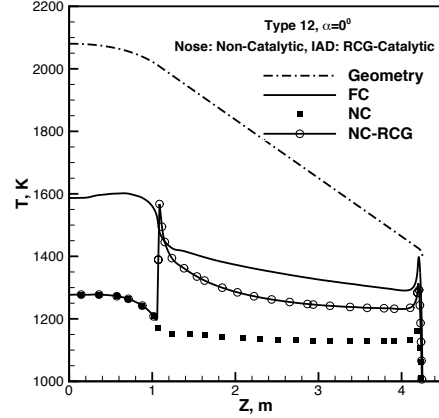
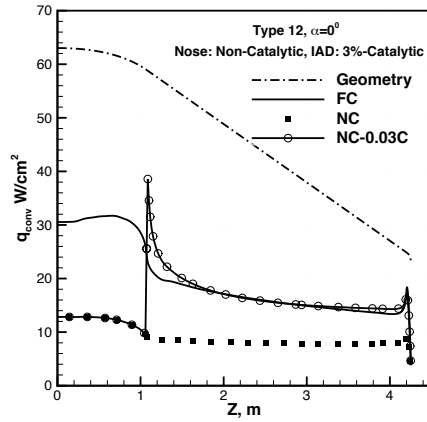(a) Surface heat flux distribution with $\gamma = 1\%$ catalysis on the IAD.
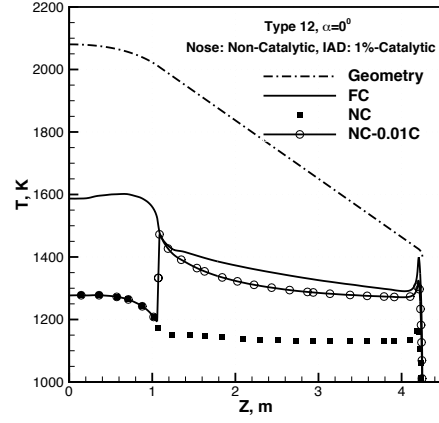
(b) Surface temperature distribution with $\gamma = 1\%$ catalysis on the IAD.
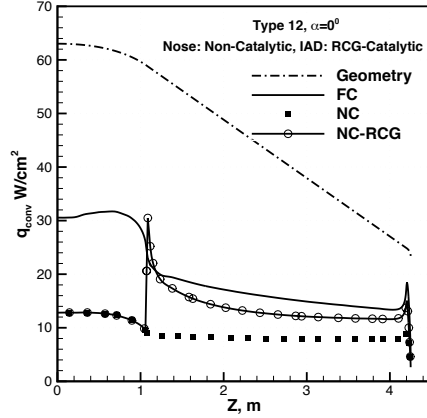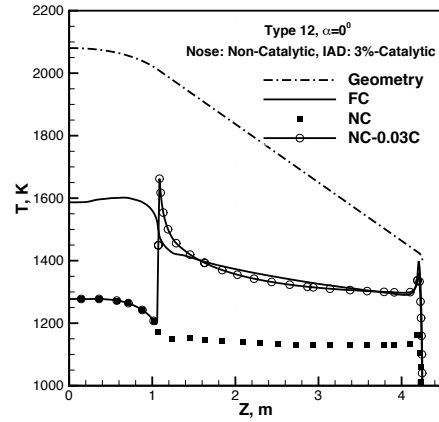
(c) Surface heat flux distribution with RCG catalysis on theIAD.

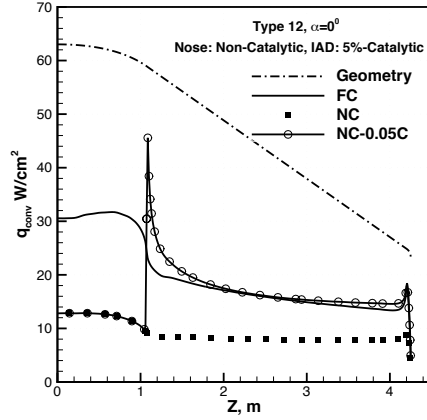(d) Surface temperature distribution with a RCG catalysis on the IAD.

(e) Surface heat flux distribution with $\gamma = 3\%$ catalysis on the IAD.
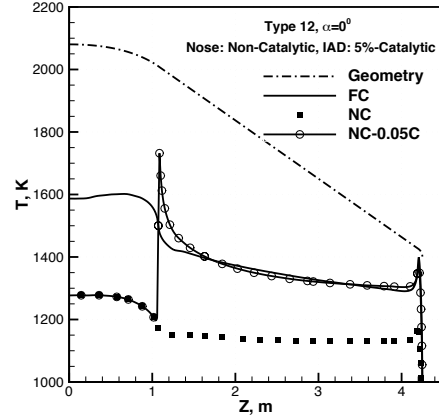
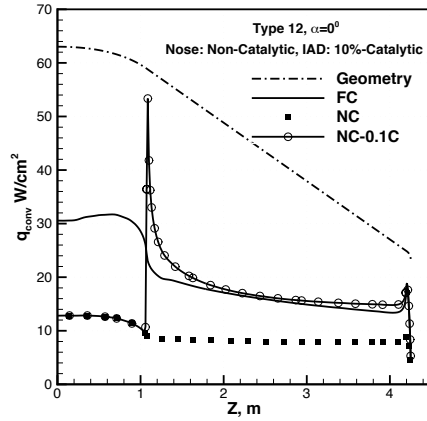(f) Surface temperature distribution with $\gamma = 3\%$ catalysis on the IAD.

Figure 13. Catalytic jump along the center body of the Type 12 geometry with a non-catalytic nose at $\alpha = 0°$.
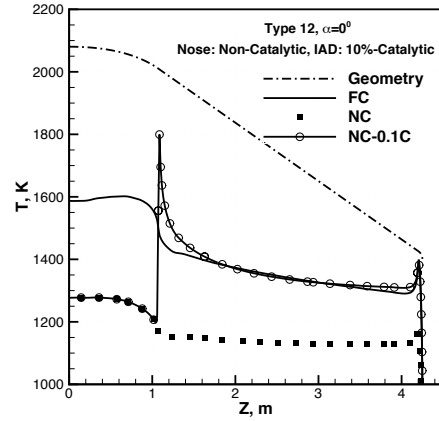
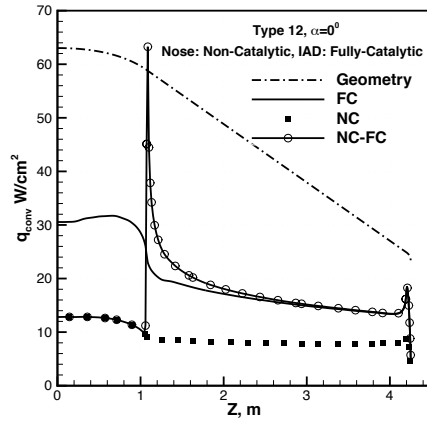(g) Surface heat flux distribution with a 5% catalytic IAD.

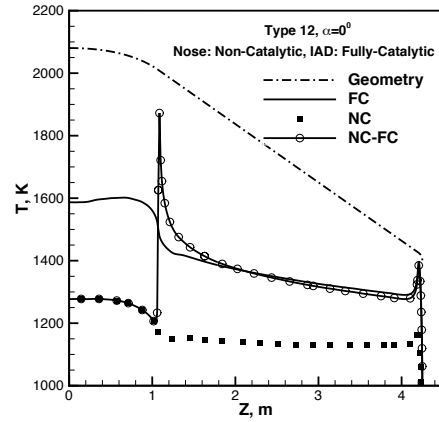(h) Surface temperature distribution with a 5% catalytic IAD.

(i) Surface heat flux distribution with a 10% catalytic IAD.

(j) Surface temperature distribution with a 10% catalytic IAD.

(k) Surface heat flux distribution with a fully-catalytic IAD.

(l) Surface temperature distribution with a fully-catalytic IAD.

Figure 13. Catalytic jump along the center body of the Type 12 geometry with a non-catalytic nose at $\alpha = 0°$(concluded.)

17

maximum temperature augmentation factor, MTAF, are defined relative
to the maximum heating value on a non-catalytic surface:

$$MCAF = \frac{q}{(q_{max})_{\gamma=0}}$$

$$MTAF = \frac{T}{(T_{max})_{\gamma=0}} \tag{2}$$

This table indicates that a 1% catalytic condition on the IAD TPS fabric
leads to a surface heat flux jump at the nose-IAD juncture in excess of
twice the non-catalytic stagnation point value. The surface temperature,
however, was less sensitive to the catalytic jump.

Sensitivity of the nose surface catalysis to the catalytic jump was
also studied by repeating the above analyses with a RCG-catalytic nose
and several IAD catalytic conditions ranging from 1% to 100%. A case
with a uniform nose-IAD RCG-catalytic condition was also considered.
Figure 14 shows the surface heat flux and temperature variations along
the centerline of the HEART geometry. Comparing the RCG-catalytic
nose results with the one presented with a non-catalytic nose in Figure
13, show that the RCG-catalytic nose had much more moderate surface
heat flux jumps than the non-catalytic nose. For example, the maximum
surface catalytic augmentation factor, MCAF, for the RCG nose with a
10%-catalytic IAD was only about 12% compared to 424% predicted with
the non-catalytic nose. The catalytic augmentation factor for the RCG-
catalytic nose was about 1.0 for IAD catalytic surfaces with $\gamma < 0.10$.
The catalytic jump became a catalytic undershoot with IAD catalysis
less than 0.01. Table 4 provides a summary of the RCG-catalytic nose
results. A comparison of Table 3 to 4 shows that by applying a simple

Table 4. Summary of the catalytic jump analysis for the Type 12 ge-
ometry with a RCG-catalytic nose at the peak heating condition and
$\alpha = 0°$.

IAD Catalysis (γ)	$q_{max}, W/cm^2$	T_{max}, K	MCAF	MTAF
RCG	27.2	1541	1.00	1.00
0.01	27.2	1541	1.00	1.00
0.03	27.2	1541	1.00	1.00
0.05	27.3	1541	1.00	1.00
0.10	30.5	1580	1.12	1.03
1.00	34.8	1638	1.28	1.06

RCG-catalytic coating on the nose, the catalytic augmentation factor
could be reduced by as minimum of 97% as long as the IAD surface
catalytic was not more than 10%. This reduction reduced to about 93%
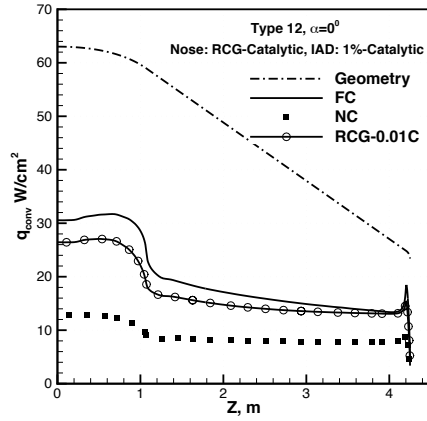with a fully-catalytic IAD.

To better understand the surface catalysis effect to the total heat
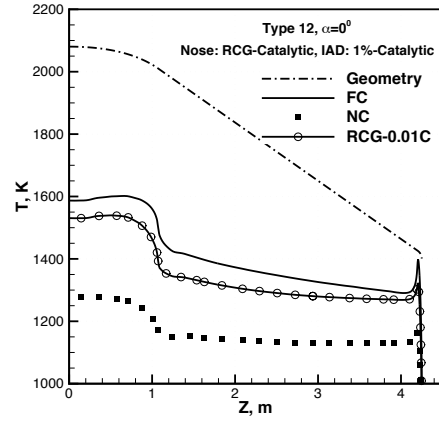flux, one could compute the contributions of the catalytic and conductive
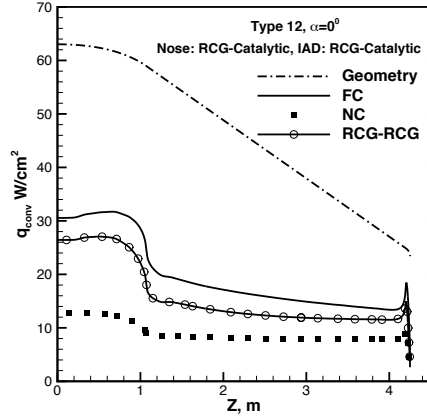
(a) Surface heat flux distribution with a RCG catalytic IAD.
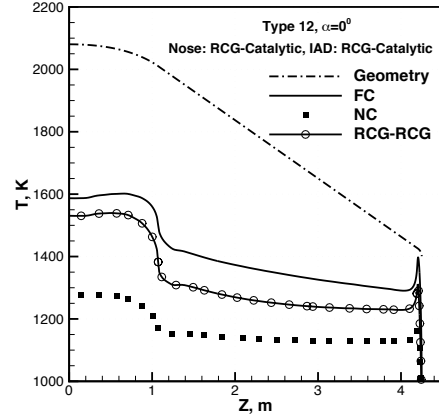
(b) Surface temperature distribution with a RCG catalytic IAD.

(c) Surface heat flux distribution with a 1% catalytic IAD.

(d) Surface temperature distribution with a 1% catalytic IAD.

(e) Surface heat flux distribution with a 3% catalytic IAD.

(f) Surface temperature distribution with a 3% catalytic IAD.

Figure 14. Catalytic jump along the center body of the Type 12 geometry with a RCG-catalytic nose at $\alpha = 0°$.

19

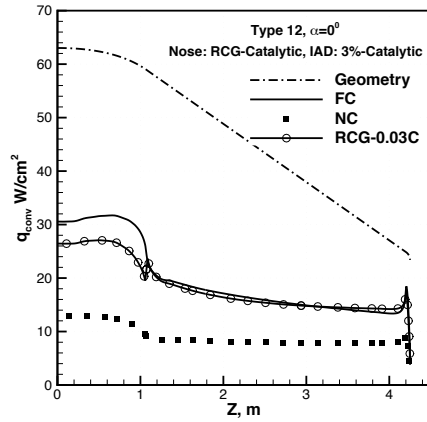(g) Surface heat flux distribution with a 5%
    catalytic IAD.

(h) Surface temperature distribution with a 5%
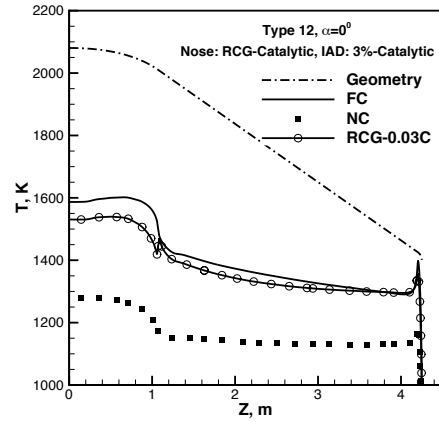   catalytic IAD.

(i) Surface heat flux distribution with a 10%
    catalytic IAD.

(j) Surface temperature distribution with a 10%
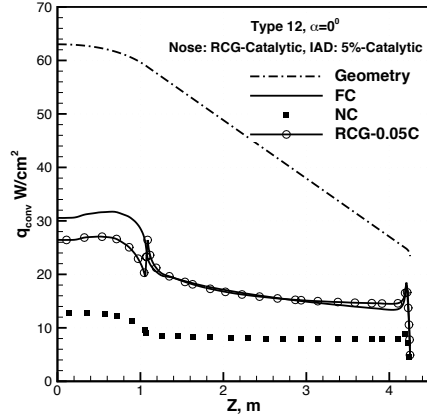   catalytic IAD.

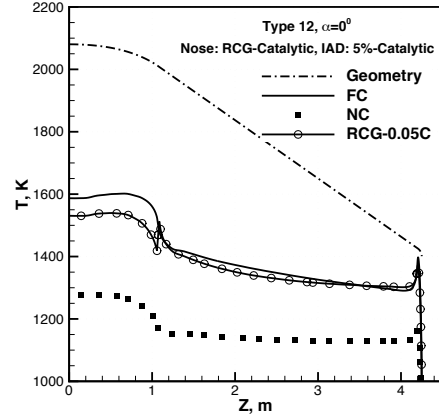(k) Surface heat flux distribution with a
    fully-catalytic IAD.

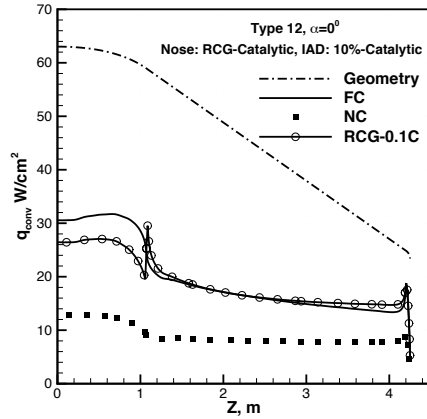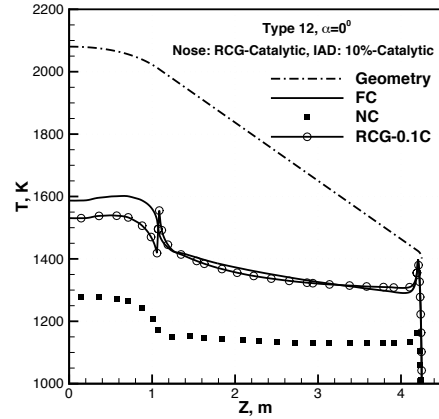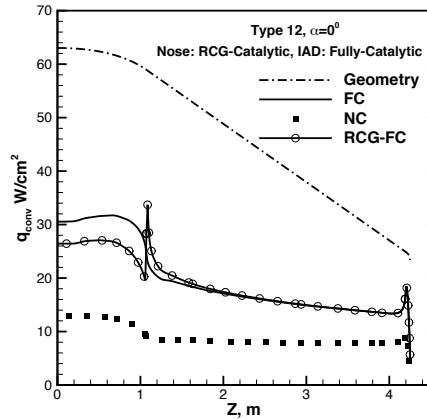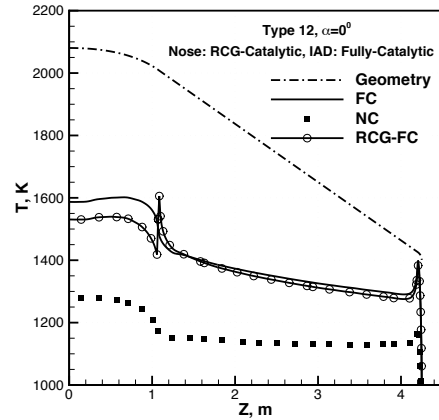(l) Surface temperature distribution with a
    fully-catalytic IAD.

Figure 14. Catalytic jump along the center body of the Type 12 geometry
with a RCG-catalytic nose at $\alpha = 0°$(concluded.)

components of the RCG nose cases, which are tabulated in Table 5. The conduction and diffusion heat fluxes are then normalized with respect to the total heat flux. These results are plotted in Figure 15.

Table 5. Catalytic and conductive contributions to the total heat flux for different IAD surface catalysis of the Type 12 geometry with a RCG nose.

IAD Catalysis (γ)	$q_{cond.}, W/cm^2$	$q_{diff.}, W/cm^2$	$q_{total}, W/cm^2$	$q_{cond.}/q_{total}$	$q_{diff.}/q_{total}$
0.00	7.9	0	7.9	1.00	0.00
RCG	8.3	3.5	11.9	0.70	0.30
0.01	8.1	5.4	13.5	0.60	0.40
0.03	7.8	6.9	14.8	0.53	0.47
0.05	7.8	7.3	15.1	0.51	0.49
0.10	7.7	7.6	15.3	0.50	0.50
1.00	7.6	7.9	15.5	0.49	0.51
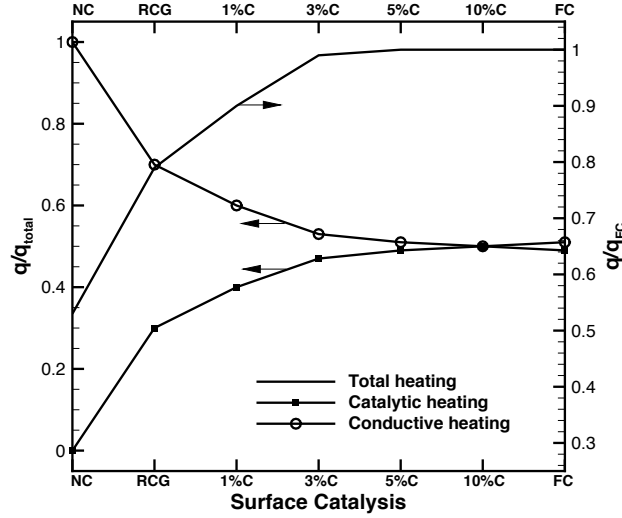
Figure 15. Catalytic and conductive heating contributions with surface catalysis for the HEART Type 12 geometry at the peak heating point.

The results showed that the catalytic (or diffusion) heat flux increased with increasing the surface catalysis while the conduction component remained fairly constant. The temperature gradient (conduction) influence to the total heat flux stayed a dominant factor until $\gamma \geq 0.05$, when the catalytic component surpassed the conduction component. However, for surface catalysis above 3%, the total heat flux reached to 100% of the corresponding fully-catalytic value. That is, the total surface heat flux stayed relatively unchanged with increasing surface catalysis efficiency. Appendix B provides the mathematical formulations related to the catalytic and conductive contributions to the heat flux and their physical

mechanisms.

6   Conclusion

A series of nose shape configurations was considered for an 8.3-m HEART entry vehicle and an optimum nose shape (Type 12) was recommended based on its surface heating at the peak heating point of an Earth entry trajectory. A deployable nose mechanism was also studied during this optimization process. Angle of attack analysis was also done on the Type 12 geometry for which the angle of attack variations of $\pm 10^o$ were shown to have a negligible effect on the overall surface heat flux.

The surface catalysis effect on heating was also studied for a two-piece nose-IAD configuration. In this configuration, the nose was not covered with the same TPS fabric as it was for the case for the IAD. Several nose and IAD surface catalyses were considered. Accordingly, it was found that TPS coating with 1-2% catalytic properties, such as RCG, on the nose reduced the TPS surface catalysis uncertainty on the IAD by at least 93% compared with fully catalytic values. For fabric TPS with surface catalysis within 5%, the minimum catalytic uncertainty reduction was about 97%. Therefore, this study recommends using a catalytic coating on the rigid nose of the HEART geometry, similar to the catalytic properties studied here, to significantly reduce the catalytic uncertainty.

Appendix A: Boundary Layer Equation and Damköhler Numbers

The results presented in Figure 13 showed that the surface heat flux increased rapidly when the surface catalysis was increased from $\gamma = 0.00$ (non-catalytic) to $\gamma = 0.01$ (1%-catalytic). However, past the nose-IAD juncture the surface heat flux rapidly decayed approaching the fully catalytic level. For example, the surface heat flux of the IAD with $\gamma = 0.01$ was about twice that of the non-catalytic surface while the corresponding value with $\gamma \geq 0.03$ was nearly the same as the fully-catalytic value. This may be explained by the gas phase recombination Damköhler number, Γ, and the heterogeneous Damköhler number, ζ, defined as [13–15, 17]:

$$\Gamma = \frac{4Sc\,k_r'T_{stg}^{\omega-2}}{(\epsilon+1)\beta_{stg}}(\frac{P_{stg}}{\bar{R}})^2 \tag{A-1}$$

$$\zeta = \frac{Sc\,\gamma\sqrt{\frac{\bar{R}T}{\pi M_{\mathrm{w}}}}}{\mu_{\mathrm{w}}}\sqrt{\frac{\rho_{\mathrm{w}}\mu_{\mathrm{w}}}{\beta_{stg}}} \tag{A-2}$$

where ϵ is the geometry related parameter, 0 for 2D and 1 for axisymmetric and 3D geometries, β is the velocity gradient at the stagnation point, and ω is the recombination rate temperature exponent.

The gas phase recombination Damköhler number, Γ, represents the relative reaction rate's speed to the flow speed. Γ is constant for a given body and set of reactions; the larger the body, the higher the Γ value. Γ, however, is independent of the surface catalysis.

The heterogeneous Damköhler number, ζ, is representative of diffusion time to surface recombination time ration and is linearly proportional to the surface catalysis γ. ζ is constant for a given surface catalysis and a free stream condition, but increases with a body size through β but at a slower rate than Γ.

These nondimentional numbers were derived by writing the non-equilibirum boundary layer equations for the species conservation and the energy in the following form [15, 17]:

$$Sc \, f\alpha' + \alpha'' = F(\Gamma) \tag{A-3}$$

$$Pr \, f\theta' + \theta'' = \frac{h_{molecule}}{C_p T_e} F(\Gamma) \tag{A-4}$$

where f is the boundary similarity variable and $()' = d()/df$. The solution to the above equations for surface heat flux, Q_w, is [15]:

$$Q_w = \underbrace{\theta'(0)}_{\text{Continuous part}} + \underbrace{\frac{Le \, h_{molecule}}{C_p T_e} \alpha'(0)}_{\text{Non-Continuous part}} \tag{A-5}$$

This solution has two parts; a continuous part and a non-continuous part. The second part, which is a function of the surface catalysis at the wall through $\alpha'(0)$, is responsible for the catalytic jump presented in Figures 13 and 14. Equation A-5 is plotted versus the gas phase recombination Damköhler number, Γ, for various heterogeneous Damköhler numbers, ζ, in Figure A-1. In this figure, the non-dimensional heat flux is defined as $Q^* = (Q - Q_{frzn})/(Q_{eq} - Q_{frzn})$. Therefore, the $Q^* = 0$ is representative of frozen heat flux while $Q^* = 1$ is the equilibrium solution.

This figure is used to demonstrate the surface catalysis sensitivity to the heat flux that was shown in Figures 13 and 14. Note that the boundary layer solution is for a very special class of problems that are somewhat different than the multi-body recombinations cases conducted for the HEART at the peak heating with a radiative equilibrium boundary condition. The solution shown in Figure A-1 is for a single-body recombination with a cold surface. Thus, the solution may only be used for demonstration and better understanding of the surface catalysis effect.

For this reason, boundary layer values and the Damköhler numbers are only extracted from the HEART CFD solutions at the stagnation point for a closer representation to the boundary layer solution. The boundary layer solution is then used to extract the nondimensional heat flux Q^*. These are tabulated for different surface catalysis in Table A-1.
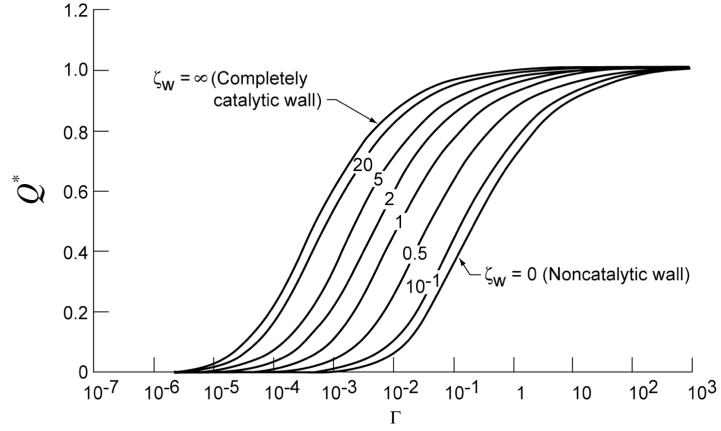
Figure A-1. Surface heat flux with Damköhler numbers; reproduced from the work of Ref. [13] (corrected the labeling.)

Table A-1. Boundary layer solution and the Damköhler numbers calculated from the HEART stagnation point at the peak heating trajectory point and $\alpha = 0^o$.

Catalytic efficiency (γ)	ζ	Γ	Q^*
0.01	0.4	0.5	0.75
0.03	1	0.5	0.80
0.05	2	0.5	0.85
0.10	4	0.5	0.90
1.00	40	0.5	1.00

24

The results in this table show a rapid increase of heat flux as the surface catalysis increases up to $\gamma = 0.03$, but this effect reaches a plateau at higher surface catalytic efficiencies. This is very similar to what is shown with the CFD analyses in Figures 13 and 14.

Appendix B: Catalytic and Conductive Heat Flux Relations w.r.t. Surface Catalysis

In Section 5, catalytic surface effect was discussed and the surface heat flux responses to the surface catalytic condition were shown. Here a more detailed understanding of the surface catalytic effects to the heat flux is provided.

The heat flux equation can be separated to account for the conduction and the diffusion contributions as

$$q_w = (\underbrace{k\frac{\partial T}{\partial y}}_{\text{Conduction}} + \underbrace{\sum_i \rho D h_i \frac{\partial c_i}{\partial y}}_{\text{Diffusion}})_w \tag{B-1}$$

where the summation is over the species. The diffusion part is indirectly a function of surface catalysis but it is directly influenced by the species gradient at the wall. The surface catalysis changes atomic and molecular species concentration at the wall, which then influences the species gradient.

To illustrate the surface catalysis effect, consider the following reaction:

$$N + N^\downarrow \to N2 \tag{B-2}$$

where $N^\downarrow$ represents upcoming atomic nitrogen toward the wall. This is illustrated schematically in Figure B-1. For this reaction, the flux of species toward the wall must be balanced with the species diffusion at the wall:
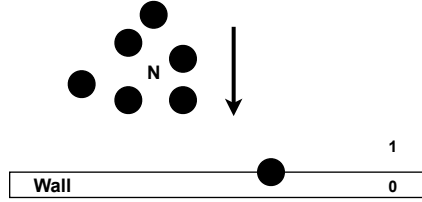

Figure B-1. Schematic of atom depositions at the wall.

$$J_N^\downarrow = J_N \tag{B-3}$$

$$\rho(\chi_N)_w \gamma \sqrt{\frac{\kappa T}{2\pi m_N}} = (\rho D)_N (\frac{\partial \chi_N}{\partial y})_w \tag{B-4}$$

25

where χ is the species mole fraction, γ is the surface catalytic efficiency, and y is the cell height. For CFD implementation purposes, $(\chi_N)_w$ may be averaged between values in the cell above the surface and the cell below the surface (pseudo cell), shown schematically in Figure B-1 as 1 and 0, respectively. The species gradient at the wall may be computed using second order differencing. After some algebra, the atoms molar concentrations in the pseudo cell are obtained as:

$$\chi_N^0 = \chi_N^1 \frac{1 - A}{1 + A} \tag{B-5}$$

where

$$A = \frac{1}{2} \frac{\Delta y}{(\rho D)_N} \rho \gamma \sqrt{\frac{\kappa T}{2\pi m_N}} \tag{B-6}$$

For a homogeneous recombination process, the molecular molar concentration at the wall is then computed knowing that the sum of the species diffusion fluxes must be zero at the wall:

$$J_N + J_{N2} = 0 \tag{B-7}$$

$$(\rho D)_N (\frac{\partial \chi_N}{\partial y})_w + (\rho D)_{N2} (\frac{\partial \chi_{N2}}{\partial y})_w = 0 \tag{B-8}$$

Discretizing the species gradients and rearranging the Equation B-8, one may obtain the molecular concentration at the psudo cells as:

$$\chi_{N2}^0 = \chi_{N2}^1 + (\chi_N^1 - \chi_N^0)\frac{(\rho D)_N}{(\rho D)_{N2}} \tag{B-9}$$

The change of species concentrations at the wall, due to the surface catalysis, indirectly affects the species rate of production throughout the boundary layer. For a thermal equilibrium condition (one-temperature), the species rate of production is presented only in the species conservation equation:

$$\frac{\partial}{\partial t}\rho_s + \frac{\partial}{\partial x^j}(\rho_s u^j) = \frac{\partial}{\partial x^j}(\rho D_s \frac{\partial c_s}{\partial x^j}) + \dot{w}_s \tag{B-10}$$

where c_s is the species s mass fraction, and $\dot{w}$ is the species mass rate of production. For generic reactions such as

$$\alpha_1 A + \alpha_2 B \rightleftharpoons \beta_1 C + \beta_2 D \tag{B-11}$$
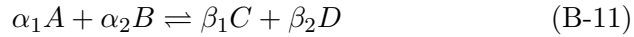
where α and β are Stoichiometric coefficients, the species mass rate of production is computed as

$$\dot{w}_s = M_s(\sum_{s=1}^{N_{react.}} (\beta_s - \alpha_s)K_{frwrd} - \sum_{s=1}^{N_{prod.}} (\beta_s - \alpha_s)K_{bkwrd}) \tag{B-12}$$

26

and the forward and backward reactions are computed as

$$K_{frwrd} = e^{a+blnT-c/T} \prod_{s=1}^{N_{react.}} (\frac{\rho_s}{M_s})^{\alpha_s} \qquad \text{(B-13)}$$

$$K_{bkwrd} = e^{a+blnT-c/T-lnK_c} \prod_{s=1}^{N_{prod.}} (\frac{\rho_s}{M_s})^{\beta_s} \qquad \text{(B-14)}$$

The equilibrium constant, K_c, which is needed for computation of the backward reaction rates, is calculated from the species Gibbs free energy, G_s, through the following equation

$$ln\,K_c = -(\sum_{s=1}^{N_{react.}} \alpha_s G_s - \sum_{s=1}^{N_{prod.}} \beta_s G_s) - \sum_s (\alpha_s + \beta_s) ln(RT) \qquad \text{(B-15)}$$

The process from the Equation B-2 through the Equation B-15 is repeated along with the surface temperature boundary condition until a convergence is reached. The same process can be expanded for multibody recombinations such as 5-species air.

The detailed analysis of surface catalysis effect on surface heat flux provides no analytical expression for the surface heat flux, unlike the boundary layer equation discussed in the Appendix A. However, this detailed process reveals more accurate information not only at the stagnation point but also on every surface point and throughout the boundary layer. This analysis also shows the non-linearity of the surface catalysis effect on the total heat flux as presented in Figure 15.

References

1. Hughes, S.J., Cheatwood, F.M., Dillman, R.A., Wright, H.S., Del-Corso, J.A., and Calomino, A.M., "Hypersonic Inflatable Aerodynamic Decelerator (HIAD) Technology Development Overview," AIAA Paper, 2011-2524, 2011.

2. Reza, S., Hund, R., Kustas, F., Willcockson, W., Songer, J., Brown, G., "Aerocapture Inflatable Decelerator (AID) for Planetary Entry," AIAA Paper, 2007-2516, 2007.

3. Hughes, S.J., Dillman, R.A., Starr, B.R., Stephan, R.A., Lindell, M.C., Player, C.J., and Cheatwood, F.M., "Inflatable Re-entry Vehicle Experiment (IRVE) Design Overview," AIAA Paper 2005-1636, 2005.

4. Mazaheri, A.R., Gnoffo, P.A., Johnston, C.O., and Kleb, B., "LAURA 5 Users Manual," NASA TM-217092-2011, 2011.

5. Hash, D., Olejniczak, J., Wright, M., Prabhu, D., Pulsonetti, M., Hollis, B., Gnoffo, P., Barnhardt, M., Nompelis, I., and Candler G., "Fire II Calculations for Hypersonic Nonequilibrium Aerothermodynamics Code Verifcation: DPLR, LAURA and US3D," AIAA Paper 2007-0605, 2007.

6. Mazaheri, A., and Wood, W.A., "Re-Entry Aeroheating Analysis of Tile-Repair Augers for the Shuttle Orbiter," AIAA Paper 2007-4148, 2007.

7. Mazaheri, A., and Wood, W.A., "Heating Augmentation for Short Hypersonic Protuberances," Journal of Spacecraft and Rockets, Vol. 46, No.2, 2009, pp.284-291.

8. Dyakonov, A.A., Schenenberger, M., Scallian, W.I., Van-Norman, J.W., Novak, L.A, and Tang, C.Y., "Aerodynamic Interference Due to MSL Reaction Control System," AIAA Paper 2009-1030, 2009.

9. Johnston, C.O., Gnoffo, P.A., and Mazaheri, A., "A Study of Ablation-Flowfield Coupling Relevant to the Orion Heatshield", AIAA Paper 2009-4318, 2009.

10. Wright, M.J., White, T., and Mangini, N., "Data Parallel Line Relaxation (DPLR) Code User Manual", NASA-TM-2009-215388, 2009.

11. Hughes, S.J., private communication, HIAD Chief Engineer, NASA Langley Research Center, Stephen.J.Hughes@nasa.gov, December 2011.

12. Gupta, R.N., Scott, C.D., and Moss, J.N., "Slip-Boundary Equations for Multicomponent Nonequilibrium Airflow," NASA Technical Paper 2452,1985.

13. Inger, G.R., "Nonequilibrium-Dissociated Boundary Layers with a Reacting Inviscid Flow," AIAA J., Vol. 1, No. 9, pp. 2057-2061,1963.

14. Inger, G.R., "Nonequilibrium Boundary-Layer Effects on the Aerodynamic Heating of Hypersonic Waverider Vehicles," Journal of Thermophysics and Heat Transfer, vol. 9, No. 4, pp. 595-604,1995.

15. Gnoffo, P.A., and Inger, G.R., "Analytic Corrections to CFD Heating Predictions Accounting for Changes in Surface Catalysis, Part II," AIAA Paper 96-4589, 1996.

16. Inger, G.R., and Baker, R.L., "Nonequilibrium Viscous Shock-Layer Heat Transfer with Arbitrary Surface Catalycity," Journal of Spacecraft and Rockets, vol. 42, No.2, pp.193-200, 2005.

17. Fay, J.A., and Riddell, F.R., "Theory of Stagnation Point Heat Transfer in Dissociated Air," Journal of Aeronautical Sciences, vol. 25, No. 2, pp. 373-386, 1958.

18. Scott, C.D., "Wall Boundary Equations with Slip and Catalysis for Multicomponent, Nonequilibrium Gas Flows," NASA TM X-58111, 1973.

REPORT DOCUMENTATION PAGE			Form Approved OMB No. 0704-0188

The public reporting burden for this collection of information is estimated to average 1 hour per response, including the time for reviewing instructions, searching existing data sources, gathering and maintaining the data needed, and completing and reviewing the collection of information. Send comments regarding this burden estimate or any other aspect of this collection of information, including suggestions for reducing this burden, to Department of Defense, Washington Headquarters Services, Directorate for Information Operations and Reports (0704-0188), 1215 Jefferson Davis Highway, Suite 1204, Arlington, VA 22202-4302. Respondents should be aware that notwithstanding any other provision of law, no person shall be subject to any penalty for failing to comply with a collection of information if it does not display a currently valid OMB control number.
PLEASE DO NOT RETURN YOUR FORM TO THE ABOVE ADDRESS.

1. REPORT DATE *(DD-MM-YYYY)* 01-05-2012	2. REPORT TYPE Technical Memorandum		3. DATES COVERED *(From - To)*
4. TITLE AND SUBTITLE HEART Aerothermodynamic Analysis			**5a. CONTRACT NUMBER**
			5b. GRANT NUMBER
			5c. PROGRAM ELEMENT NUMBER
6. AUTHOR(S) Mazaheri, Alireza			**5d. PROJECT NUMBER**
			5e. TASK NUMBER
			5f. WORK UNIT NUMBER 469904.01.06.01
7. PERFORMING ORGANIZATION NAME(S) AND ADDRESS(ES) NASA Langley Research Center Hampton, VA 23681-2199			**8. PERFORMING ORGANIZATION REPORT NUMBER** L-20142
9. SPONSORING/MONITORING AGENCY NAME(S) AND ADDRESS(ES) National Aeronautics and Space Administration Washington, DC 20546-0001			**10. SPONSOR/MONITOR'S ACRONYM(S)** NASA
			11. SPONSOR/MONITOR'S REPORT NUMBER(S) NASA/TM-2012-217568

12. DISTRIBUTION/AVAILABILITY STATEMENT
Unclassified - Unlimited
Subject Category 18
Availability: NASA CASI (443) 757-5802

13. SUPPLEMENTARY NOTES

14. ABSTRACT

This paper presents an assessment of the aerothermodynamic environment around an 8.3 meter High Energy Atmospheric Reentry Test (HEART) vehicle. This study generated twelve nose shape configurations and compared their responses at the peak heating trajectory point against the baseline nose shape. The heat flux sensitivity to the angle of attack variations are also discussed. The possibility of a two-piece Thermal Protection System (TPS) design at the nose is also considered, as are the surface catalytic affects of the aeroheating environment of such configuration. Based on these analyses, an optimum nose shape is proposed to minimize the surface heating. A recommendation is also made for a two-piece TPS design, for which the surface catalytic uncertainty associated with the jump in heating at the nose-IAD juncture is reduced by a minimum of 93%. In this paper, the aeroshell is assumed to be rigid and the inflatable fluid interaction effect is left for future investigations.

15. SUBJECT TERMS

CFD; HIAD; Hypersonic; Inflatable

16. SECURITY CLASSIFICATION OF:			17. LIMITATION OF ABSTRACT	18. NUMBER OF PAGES	19a. NAME OF RESPONSIBLE PERSON STI Help Desk (email: help@sti.nasa.gov)
a. REPORT	b. ABSTRACT	c. THIS PAGE			
U	U	U	UU	34	19b. TELEPHONE NUMBER *(Include area code)* (443) 757-5802

Standard Form 298 (Rev. 8-98)
Prescribed by ANSI Std. Z39.18